Effect of intergranular glass films on the electrical conductivity of 3Y-TZP

M. Gödickemeier, B. Michel, A. Orliukas, P. Bohac, K. Sasaki, and L. Gauckler
Nichtmetallische Werkstoffe, ETH Zürich, CH-8092 Zürich, Switzerland

H. Heinrich, P. Schwander, and G. Kostorz
Institut of Applied Physics, ETH-Zürich, CH-8093 Zürich, Switzerland

H. Hofmann and O. Frei
Alusuisse Lonza Services AG, CH-8212 Neuhausen, Switzerland

(Received 3 June 1993; accepted 11 January 1994)

The electrical conductivity of 3Y-TZP ceramics containing SiO_2 and Al_2O_3 has been investigated by complex impedance spectroscopy between 500 and 1270 K. At low temperatures, the total electrical conductivity is suppressed by the grain boundary glass films. The equilibrium thickness of intergranular films is 1–2 nm, as derived using the "brick-layer" model and measured by HRTEM. A change in the slope of the conductivity Arrhenius plots occurs at the characteristic temperature T_b at which the macroscopic grain boundary resistivity has the same value as the resistivity of the grains. The temperature dependence of the conductivity is discussed in terms of a series combination of RC elements.

I. INTRODUCTION

Thin intergranular glass films which are composed of SiO_2, Al_2O_3, and Y_2O_3 are formed in Y-TZP ceramics at high sintering temperatures.[1–7] They promote sintering of the starting powders as well as grain growth during the post-annealing process and affect the electrical and mechanical properties of Y-TZP ceramics.[8–11] It has been shown that the equilibrium film thickness is limited to about 1–2 nm,[4,12–14] and excess amounts of glass segregate in grain triple junctions, in pores, and on the surface of the specimens.[4,5,11] The equilibrium width of intergranular films depends on the corresponding interfacial energies and on the viscosity of the glass phase at the temperature of sintering or post-annealing.[15,16] A surplus of Al_2O_3 is proposed to act as a scavenger for SiO_2, removing it from grain boundaries.[17,18] The glass phase can also be partially squeezed out from the grain boundaries to three grain pockets by applying a compressive stress.[19] Accordingly, in hot-pressed specimens of Y-TZP at 1823 K some "clean" grain boundaries were observed, which did not contain any detectable intergranular phase.[16]

The Arrhenius plots [$\log(\sigma T)$ vs $1/T$] of the total (dc) conductivity of zirconia-based solid electrolytes often exhibit a change of slope at 800–1200 K, owing to a decrease in activation energy at high temperatures.[20–22] Rather controversial explanations for the origin of this curvature of the Arrhenius plots have been given in the literature.[23–30] The majority of studies suggests that in the low-temperature region immobile associated complexes, such as $[Y'_{Zr}V''_O]^{\cdot}$, are formed between extrinsic oxygen vacancies and oppositely charged dopant ions. The thermal dissociation of these complexes would require a supplementary energy in addition to the activation energy for the simple migration of "free" charge carriers.[23–26]

According to this concept, three general stages of the ionic conductivity are proposed to exist in solid electrolytes as a function of temperature.[27,31] The first bend in the Arrhenius curve occurs on cooling from the high temperature "intrinsic stage I" to the "extrinsic-dissociated stage II" at which all extrinsic charge carriers are claimed to be mobile. The intrinsic stage exhibits a higher activation energy that is necessary not only for the migration but also for the formation of intrinsic charge carriers. At the transition temperature I → II, the concentration of thermally activated intrinsic charge carriers becomes equal to the total concentration of extrinsic charge carriers generated by doping. Another bend in the Arrhenius plot at lower temperatures is assumed to occur from the extrinsic-dissociated stage II to the "extrinsic-associated stage III". Since the activation energy of the low-temperature stage III includes an additional energy for the dissociation of defect complexes, it is again higher than the activation energy of the middle stage II, which corresponds to the energy for the migration of free extrinsic charge carriers only. At the temperature of the second transition (II → III), the concentration of thermally dissociated, "mobile" extrinsic charge carriers is supposed to be equal to the concentration of extrinsic charge carriers which are still associated and "immobile". Supposing association energies of 0.2–0.5 eV, Nowick and Park[27] have calculated the temperature at

which a half of the total amount of extrinsic oxygen vacancies would be free. They suggested this temperature to be the lower "break point temperature" of the Arrhenius plots.

Other authors have interpreted the slope change of Arrhenius plots (stages II to III) to be due to changing from the volume-controlled conductivity of the grains, prevailing at high temperatures, to the grain-boundary-controlled conductivity at low temperatures,[28–30] due to microcracking,[21] phase transformation,[28,32] or even as a mere artifact of the experimental technique.[33]

A formation of dopant-vacancy associates in the proposed "extrinsic-associated range (III)" was claimed to reduce the concentration of "free" charge carriers in stabilized zirconias with increasing dopant content.[23,34–36] Assuming associated defect complexes, Weller and Schubert[26] have questioned the current accepted values of intragrain bulk conductivities and their activation energies obtained by impedance spectroscopy measurements and proposed a revision of the classical interpretation of this widely used experimental method.[28,37–39] On the other hand, no difference between "mobile" and "immobile" lattice defects was found in the studies of Orliukas *et al.*,[40] Casselton,[41] and Anantha-padmanabhan *et al.*[42]

To explain the blocking effect of the grain boundaries, two models, in terms of an electrical connection of the bulk and the segregated grain boundary material either in series or parallel, are given in the literature.[8,9,14,37,43,44] According to the first, "brick layer" or series model,[8,9,20] conducting grains are separated by a continuous film of a less conducting grain-boundary phase. The second, "easy path" or parallel model,[45,46] assumes only a partial blocking of the current path due to a discontinuous distribution of an insulating phase between conducting grains.

In the present work the intergrain relaxation of the ionic conductivity has been studied by complex impedance spectroscopy on 3Y-TZP specimens containing different amounts of the grain boundary glass phase. The purpose of this study was to clarify the relationship between the chemical composition of the starting material which determines the amount of the intergranular phase and the electrical properties of 3Y-TZP ceramics and to provide a better understanding of the bend in Arrhenius plots of total conductivity observed in zirconia-based solid electrolytes at 800–1200 K.

II. EXPERIMENTAL

The compositions of the investigated 3Y-TZP samples are shown, with respect to their SiO_2–Al_2O_3 content, in Fig. 1. The samples lie along the lines A, B, C, D, and E, which correspond to the SiO_2/Al_2O_3 ratios of 1/0, 4/1, 1/1, 1/4, and 0/1, respectively. The

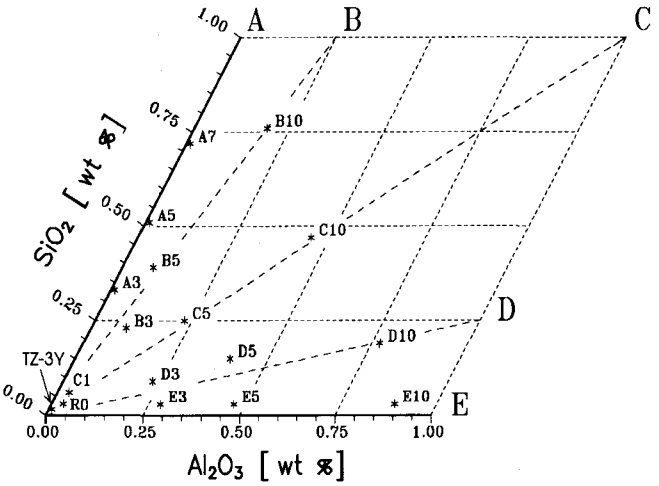

FIG. 1. The compositions of 3Y-TZP samples with respect to SiO_2–Al_2O_3 impurities.

total amount of both oxides is given approximately in tenths of a weight % by the sample number and varies from about 0.1 wt. % for the C-1 sample to 1 wt. % in samples B-10, C-10, D-10, and E-10. The coprecipitated 3Y-TZP powder without impurity additions has been considered as the reference (sample R-0). For comparison, a sample from the pure commercial powder TZ-3Y (Toshoh Corporation, <0.005 wt. % SiO_2 and <0.002 wt. % Al_2O_3), which is designated as TZ-3Y, as well as a very contaminated sample F-46 containing 4.6 wt. % of both impurities in total have also been investigated.

All 3Y-TZP sintered specimens were prepared using coprecipitated ultrafine powders. The SiO_2 and Al_2O_3 impurities were introduced as $SiCl_4$ and $AlCl_3$ into the solution of $ZrOCl_2$ and YCl_3 before the wet-chemical precipitation. The only exception is the sample F-46, which was prepared by mixing of the reference powder R-0, calcined at 1023 K, with a fine SiO_2 powder (Aerosil OX50, Degussa) in an attritor mill. All other coprecipitated powders were calcined at 1223 K for 8 h. The calcined powders have specific surface areas between 11 and 36 m^2/g. Their chemical analysis is shown in Table I.

The starting powders were uniaxially cold pressed at 100 MPa and sintered for 1 h in air at 1773 K. The density of all sintered samples was >96% of the theoretical value. The ceramic microstructures were revealed by thermal etching of polished specimens at 1720 K for 30 min. Only the tetragonal crystalline phase was detected by x-ray diffraction after sintering. The average linear grain size parameter, l (see Table II), was determined as the mean intercept length on SEM photomicrographs (JEOL, JEM-6400) by the linear-intercept method.[47,48] It varies in the range of 300 nm to 430 nm.

TABLE I. Chemical composition of Y-TZP powders.

Sample	$SiO_2 : Al_2O_3$ ratio	SiO_2	Al_2O_3	Y_2O_3 (wt.%)	Na_2O	Cl^-	Σ imp.	BET (m^2/g)
TZ-3Y	2.50	<0.005	<0.002	5.140	0.023	<0.01	0.10	15.2
R-0	> 1	0.03	<0.03	5.33	0.08	0.01	0.15	11
A-3	>33	0.33	<0.01	5.41	0.04	0.01	0.39	18
A-5	>51	0.51	<0.01	5.38	0.05	0.07	0.64	21
A-7	>72	0.72	<0.01	5.40	0.05	0.02	0.80	24
B-3	2.56	0.23	0.09	5.23	0.01	0.01	0.34	17
B-5	4.88	0.39	0.08	5.32	0.01	0.01	0.49	19
B-10	4.00	0.76	0.19	5.21	<0.01	<0.01	0.97	21
C-1	2.00	0.06	0.03	5.38	0.02	0.13	0.24	17
C-5	1.09	0.25	0.23	5.25	0.04	0.01	0.53	20
C-10	1.04	0.47	0.45	5.33	0.03	0.01	0.96	18
D-3	0.39	0.09	0.23	5.35	0.03	0.01	0.36	21
D-5	0.38	0.15	0.40	5.52	0.04	0.01	0.60	19
D-10	0.25	0.19	0.77	5.41	0.02	0.01	0.99	19
E-3	<0.11	<0.03	0.28	5.31	0.01	0.01	0.33	16
E-5	<0.06	<0.03	0.47	5.27	0.03	0.01	0.54	15
E-10	<0.03	<0.03	0.89	5.21	0.03	0.01	0.96	17
F-46	2.23	3.15	1.41	6.62	0.07	0.01	4.64	36

Complex impedance spectroscopy at alternating fields of variable frequency[37–39,45] has been used to distinguish between the intragrain and the grain boundary contribution to the charge transport. The total impedance of the ceramic specimens originates from the impedance contribution of the grains and from interfacial effects on grain boundaries and electrodes. A simplified equivalent circuit consists of three resistors in series, each shunted by a capacitor in parallel.

The complex impedance measurements using a PC-controlled HP Precision LCR meter 4284A were carried out between 500 and 1200 K in air, on sintered cylindrical samples 10 mm in diameter and 1–2 mm thick, using the two-point probe technique. The frequency range was 40 Hz to 1 MHz. Platinum electrodes were painted on the specimens by applying a conductive platinum paste (Demetron 308A) and sintered onto the surface at 1073 K. The temperature was controlled to ±2 °C.

TABLE II. Linear average grain sizes of annealed 3Y-TZP samples.

	Grain size l (nm)		
Sample	Time: 1 h	5 h	10 h
TZ-3Y	300		
R-0	320	510	580
A-3	320		
A-5	360		
A-7	350	440	560
B-3	430		
B-5	380		
B-10	390	810	960
C-1	340	510	660
C-5	380	580	810
C-10	380	1010	1280
D-3	380		
D-5	430		
D-10	380	620	1060
E-3	390		
E-5	410		
E-10	410	470	720
F-46	300		

III. RESULTS AND DISCUSSION

A. Impedance spectroscopy

An example of the frequency dependence of the real part of the specific electrical impedance, $\rho' = Z' \cdot L/A$, where $Z' = U_R/I_R$ is the real part of the complex impedance $Z = Z' + iZ''$, L is the sample length, and A the electrode area, is shown in Fig. 2 (sample E-10).

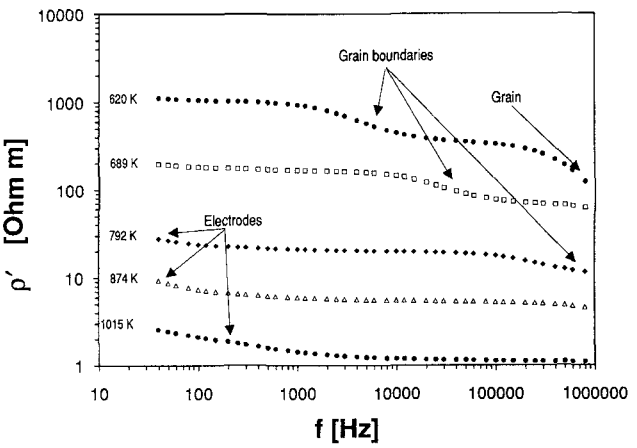

FIG. 2. Grain, grain boundary, and electrode dispersions of the real part of complex specific impedance (sample E-10).

The relaxation dispersions of individual impedance contributions (grains, grain boundaries, and electrodes) shift toward higher frequencies with increasing temperature. This indicates that these dispersions are thermally activated. Usually it is not possible to observe all three dispersions simultaneously, due to a limited frequency range used in this study (40 Hz–1 MHz). At temperatures below 500 K only the grain dispersion can be seen at high frequencies.[40] The grain boundary and the electrode dispersion are too slow to be detected at this temperature. In the medium temperature range (500 K–800 K), we can observe two dispersions, that of the grains and that of the grain boundaries. Finally, above 800 K the intragrain dispersion shifts out of the frequency window and the sluggish dispersion due to the slower electrode processes becomes visible.

In Fig. 3 the frequency dependence of the specific imaginary impedance contribution, $\rho'' = Z'' \cdot L/A$, is shown. From this figure the individual dispersion regions of grains, grain boundaries, and electrodes can be seen more distinctly.

The complex impedance data can be displayed in the complex impedance plane with real part ρ' as the abscissa and the imaginary part ρ'' as the ordinate (Cole–Cole diagram). A typical complex impedance spectrum of 3Y-TZP (sample E-10) at a medium temperature of 596 K is shown in Fig. 4. Since the time constants (τ = RC) of individual RC-elements differ by orders of magnitude, individual semicircles of the grains and that of the grain boundaries can clearly be distinguished in this temperature range. The real specific impedance sections between the distinct minima in the imaginary part ρ'' reveal the macroscopic specific resistivities of the grains (ρ'_G) and the grain boundaries (ρ'_{GB}), respectively. The macroscopic specific resistivity of the grain boundaries is equal to the difference between the total (dc) specific resistivity of the sample (ρ_T) and the macroscopic specific resistivity of the grains: $\rho'_{GB} = \rho_T - \rho'_G$. Moreover, from the maximum of imaginary impedance ρ'' at the top of each semicircle, the relaxation frequency ω of the corresponding process can be determined from the relation $\omega\tau = 1$, where $\omega = 2\pi f_R$, is the angular frequency [rad · s^{-1}], f_R the corresponding frequency of the applied electrical ac-field [Hz], and τ = RC the time constant of the relaxation circuit.

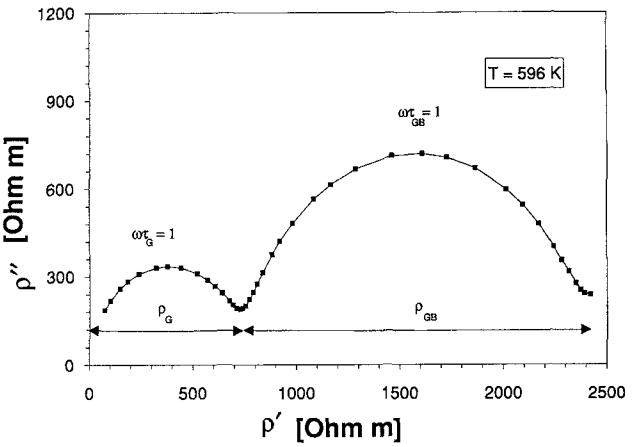

FIG. 4. Complex impedance diagram at 596 K (sample E-10).

B. Microstructure

The microstructures of the sintered 3Y-TZP specimens reveal for samples TZ-3Y, R-0, C-1, D-3, and the whole E series only very small amounts of the glass phase in triple points. On the other hand, all samples of both the B and C series as well as samples D-5 and D-10 contain large glass pockets surrounded by cubic grains (Fig. 5). Segregations of the glass phase at triple points can also be observed in samples of the A series containing silica additions without alumina.

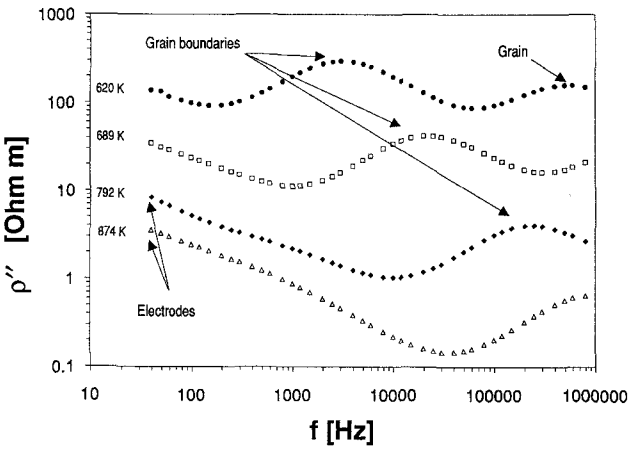

FIG. 3. Frequency dependence of imaginary part of complex specific impedance (sample A-1).

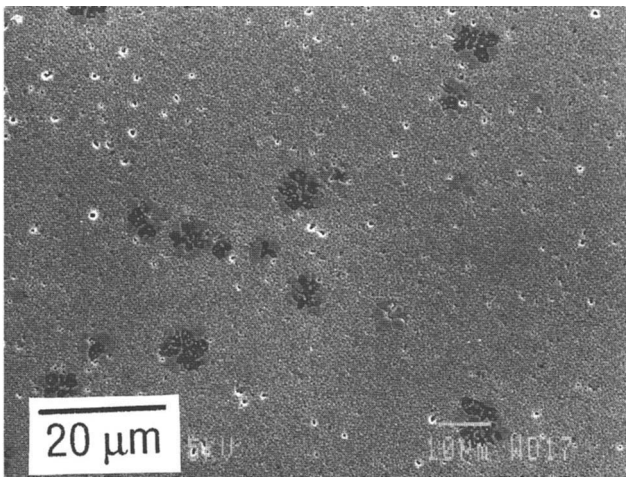

FIG. 5. Glass segregations after sintering (sample B-10).

The annealing of selected samples at 1773 K for 5 and 10 h at 1773 K caused the separation of the tetragonal and cubic phase and a gradual grain coarsening. The linear average grain sizes, l, are given as a function of annealing time in Table II. When the tetragonal grains reach a critical size, the tetragonal zirconia transforms on cooling to the monoclinic phase. This phase transition, which occurs in specimens annealed longer than 20 h, is accompanied by the formation of numerous microcracks and causes an abrupt increase of the grain boundary resistivity due to the partial blocking of the conduction path by microcracks. From Fig. 6 the development of the microstructure around a glass pocket during annealing of the B-3 sample is visible.

High resolution electron micrographs (Philips CM 30 at 300 kV, super twin lens, $C_s = 1.1$ mm, LaB_6 cathode) of grain boundary regions revealed in all samples homogeneous amorphous films about 0.5–2 nm thick. No "clean" grain boundaries without intergranular phase have been observed, even in the E series. In 3Y-TZP samples containing a large amount of the glass phase (C-5, B-10), the excess of the glass phase accumulates at three-grain pockets and at the surface. Figure 7 shows a three-grain junction area of the sample C-10 and an intergranular glass layer about 1–2 nm thick. The EDX and PEELS (parallel electron energy loss spectroscopy) analysis of the glass in triple grain junctions and in large multi-grain pockets showed that the segregated amorphous phase contains oxides of all four elements, Si, Al, Y, and Zr, except that in samples with both low SiO_2/Al_2O_3 ratio and low total impurity content no Y and Zr, and in the A series also no Al, could be detected. The glass phase in pockets of the C-10 sample consists of 42 wt.% SiO_2, 22 wt.% Al_2O_3, 21 wt.% Y_2O_3, and 15 wt.% ZrO_2 (Fig. 8). This composition of the grain boundary phase is in a good agreement with the results of other authors,[1,3,5,14,16] which also showed the presence of Si, Al, Zr, and a high concentration of Y.

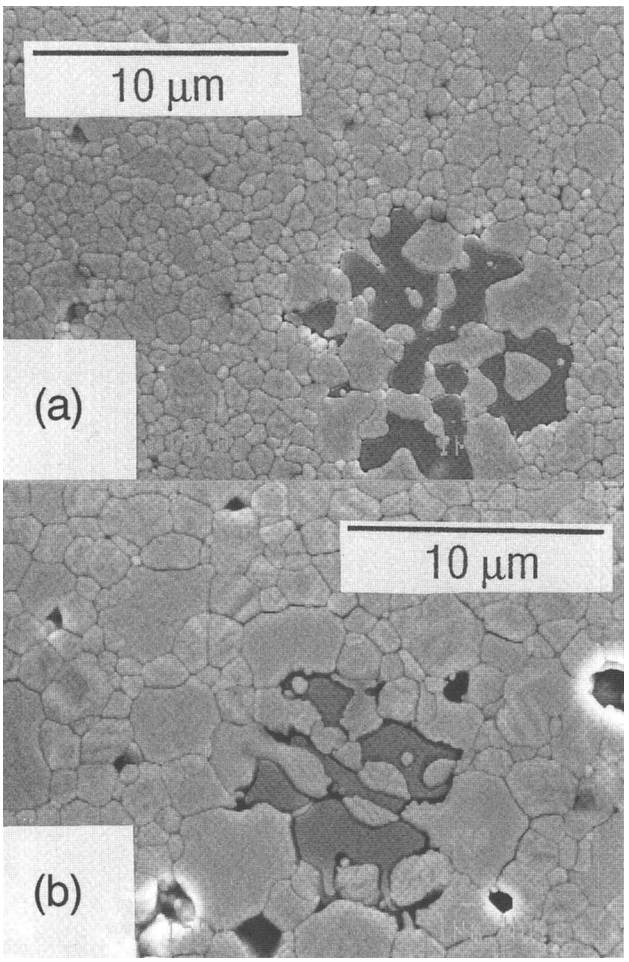

FIG. 6. Microstructure development during annealing at 1773 K (sample A-5): (a) 10 h and (b) 30 h.

C. The "brick layer" model

To analyze the electrical conductivity of a ceramic material in which the intergranular phase is present as a three-dimensional connected network of continuous films, the brick layer model can be used.[8,9,14,49,50] According to the brick-layer model, it is assumed that the bulk material consists of conducting grains, cubes with an edge length a, separated by a thin homogeneous grain boundary layer of low conductivity of the thickness δ_{gb}. Since $\delta_{gb} \ll a$ and $\sigma_{GB} \ll \sigma_G$, the parallel conduction along the grain boundaries can be neglected. The equivalent electrical circuit consists then of a simple series combination of two RC-elements (grain and grain boundary). The total (dc) resistance of the sample, $R_T = R_G + R_{GB}$, is the sum of the resistance of grains R_G and grain boundaries R_{GB}. Usually the macroscopic specific conductivities σ_T', σ_G', and σ_{GB}' are calculated from resistivity values, using the relation:

$$\sigma_i' = 1/\rho_i' = 1/(R_i \cdot L_T/A_T),$$

where $L_T = L_G + L_{GB} = n(a + \delta_{GB})$ is the total length of the sample between the electrodes, $n = L_T/a$ is the number of grain boundaries perpendicular to the current direction, and $A_T = A_G + A_{GB}$ is the total cross-section area of the sample. Since $L_{GB}/L_T = \delta_{gb}/(a + \delta_{gb})$, it can easily be shown that the length fraction of grain boundaries L_{GB} amounts to $L_T \cdot \delta_{gb}/(a + \delta_{gb}) \cong L_T \cdot \delta_{gb}/a$ and that of grains L_G to $L_T \cdot a/(a + \delta_{gb}) \cong L_T$. For the cross section of the current path through the area fractions of grains A_G, we obtain:

$$A_G = A_T \cdot a^2/(a + \delta_{gb}/2)^2 \cong A_T \cdot a/(a + \delta_{gb}) \cong A_T.$$

Omitting the parallel grain boundary conduction path along the length of the sample, the microscopic specific

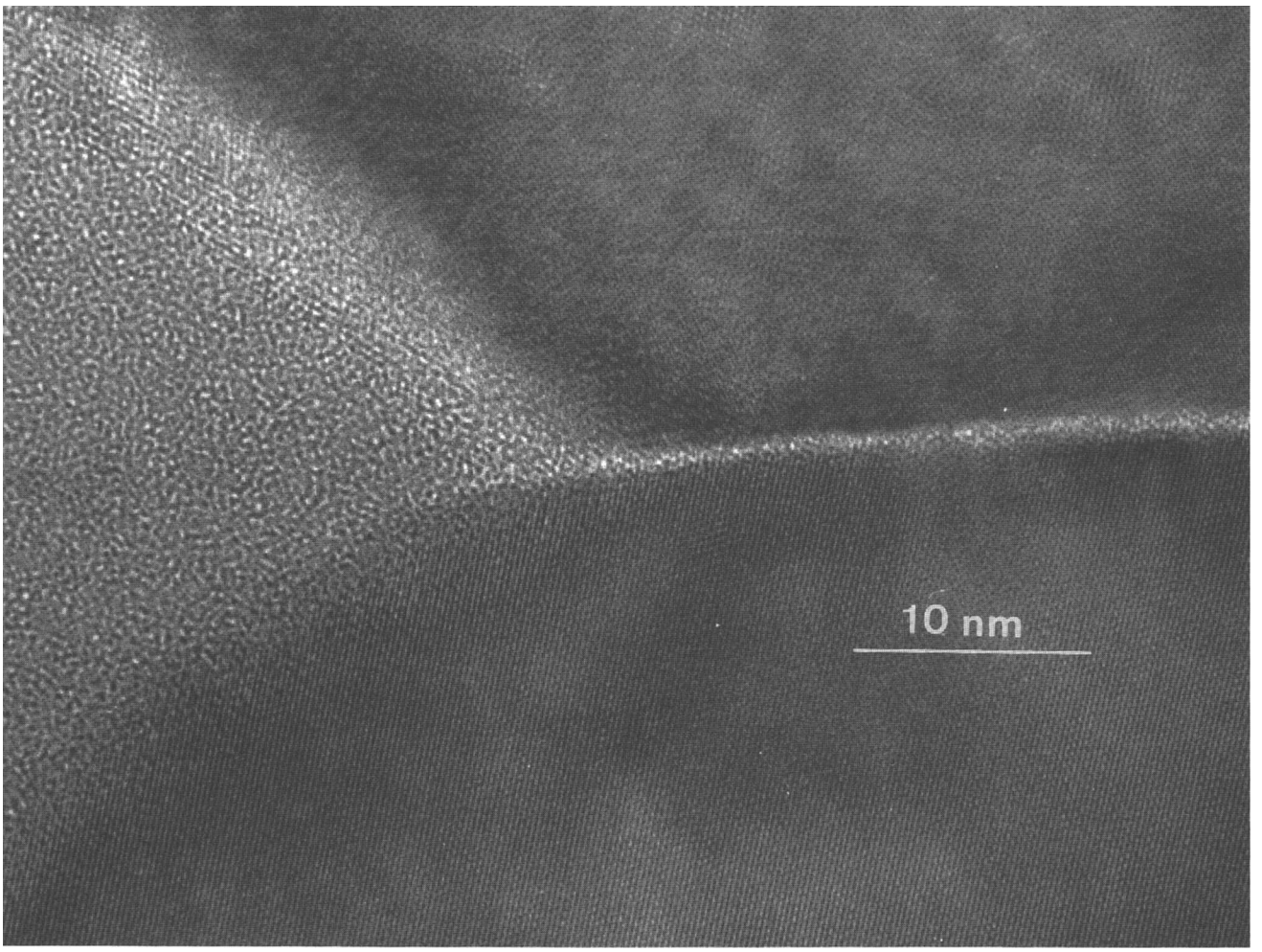

FIG. 7. HREM of a triple-point junction and an intergranular glass film (sample C-10).

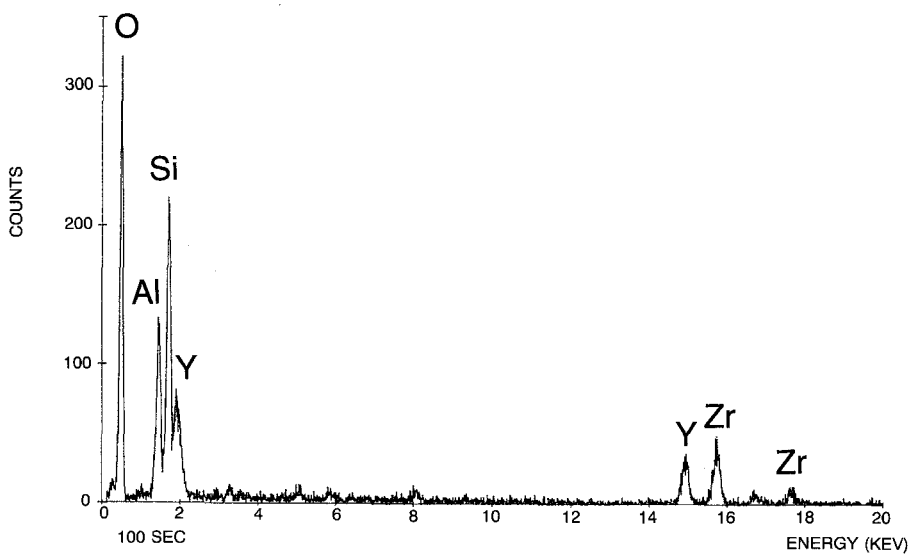

FIG. 8. EDX analysis of the glass phase segregated in a large pocket (sample C-10).

conductivity of the grain and grain boundary material at low contents of glass phase ($a \gg \delta_{gb}$) is then given by,

$$\sigma_G = \sigma'_G \quad \text{and} \quad \sigma_{GB} = \sigma'_{GB} \cdot \delta_{gb}/a \qquad (1)$$

In order to eliminate the size effect of ceramic grains, the macroscopic specific grain boundary resistivities, $\rho'_{gb} = R_{GB} \cdot A_T/L_T$, have been converted to the normalized macroscopic resistivities per unit area of the grain boundary surface,[51] r_{GB}, according to the relation,

$$r_{GB} = \rho'_{GB} \cdot a = \rho_{GB} \cdot \delta_{gb},$$

where $a = 1.5l$ is the corresponding cube edge length derived from the linear average grain size of the ceramic sample, l.[47,48] The microscopic specific resistivity of the grain boundary glass material, $\rho_{GB} = R_{GB} \cdot A_T/L_{GB}$, is then the ratio of the macroscopic resistivity per unit area r_{GB} to the grain boundary thickness $\delta_{GB}(\rho_{GB} = r_{GB}/\delta_{GB})$. In case the thickness of the intergranular glass films is known, the microscopic permittivity of the grain boundary material, ϵ_{GB}, can also be derived from the macroscopic grain boundary capacitance, C_{GB} (see Table III), according to the relationship:

$$C_{GB} = \tau/\rho'_{GB}.$$

Using the "brick layer" model,[8,14] we obtain:

$$\epsilon_{GB} = \sigma'_{GB} \cdot \delta_{GB}/(a2\pi f_R \epsilon_0) = C_{GB}/\epsilon_0 \cdot (\delta_{GB}/a), \qquad (2)$$

where $\epsilon_0 = 8.85$ pF/m is the permittivity of free space. Table III summarizes our experimental results on the electrical properties of grain boundaries at 673 K.

Figure 9 shows the relationship between the normalized grain boundary resistivity r_{GB} at 673 K and the content of total impurities. Neither the total impurity concentration nor the increasing SiO_2 content alone are responsible for the increase of the grain boundary resistance. Much more important is the combination of the appropriate impurities which determines the amount of the glass phase, especially the SiO_2/Al_2O_3 ratio (see Table I). The normalized grain boundary resistivity of both series A and E, to which only one of the glass components, SiO_2 or Al_2O_3, has been added, remains almost as low as the pure standard material (R-0) even at high total additive levels. On the other hand, the B, C, and D series containing both SiO_2 and Al_2O_3 exhibit relatively high normalized intergrain resistivities as soon as the total additive content exceeds a threshold value of about 0.3–0.5 wt. %. Already 0.2 wt. % of silica leads to a dramatic increase of the normalized grain boundary resistivity if enough alumina is present in the sample. The resistivities remain then constant at higher impurity levels.

Figure 10 shows the dependence of normalized resistivity of intergrain films on the SiO_2/Al_2O_3 ratio. The highest resistivities are found in samples containing both impurities in the SiO_2/Al_2O_3 ratio of 1/1 to 3/1.

Pure silica does not melt at the sintering temperature. Additional oxides, especially alumina and yttria, are necessary for the formation of the liquid phase at this temperature. We can assume that the appropriate amounts of Y_2O_3 and ZrO_2 are supplied by the matrix to form the glass melt. The glass-forming region of the ternary SiO_2–Al_2O_3–Y_2O system,[52,53] which

TABLE III. Relevant parameters of the grain boundaries in 3Y-TZP samples at 673 K.

Sample	Macroscopic specific resistivities		Time constant, τ (10^{-6} s)	Capacity, C_{GB} (nF/m)
	ρ'_{GB} (ohm · m)	r_{GB} (10^{-6} ohm · m^2)		
TZ-3Y	80	36	3.98	50
R-0	100	48	7.96	80
A-3	200	96	17.67	88
A-5	250	135	15.92	64
A-7	200	105	15.92	80
B-3	850	548	53.00	62
B-5	900	513	63.66	71
B-10	1050	614	69.23	66
C-1	320	163	18.78	59
C-5	1800	1026	127.32	71
C-10	1750	998	106.16	61
D-3	160	91	10.66	66
D-5	830	535	63.66	77
D-10	670	382	31.83	48
E-3	320	187	19.89	62
E-5	170	105	13.21	78
E-10	180	111	13.21	74
F-46	2480	1116	79.58	32

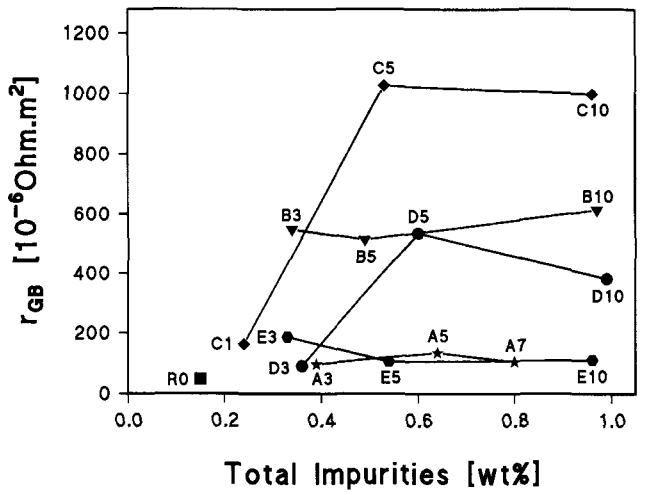

FIG. 9. Normalized grain boundary resistivity at 673 K as a function of impurity content.

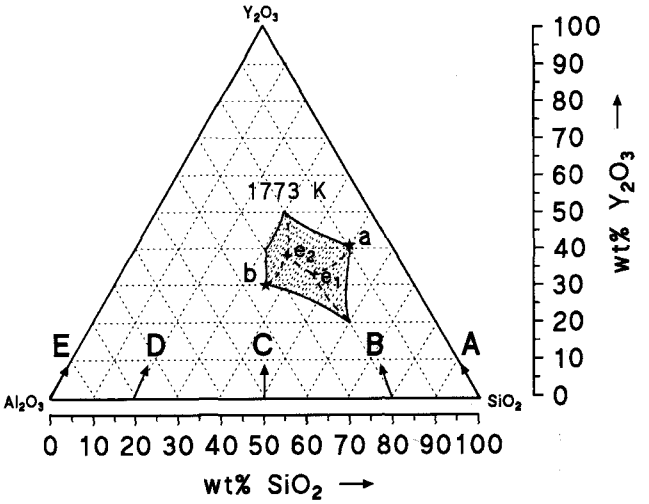

FIG. 11. Region of glass-forming melts in the $SiO_2-Al_2O_3-Y_2O$ system[52] at 1773 K.

is liquid at the sintering temperature of 1773 K, is shown in Fig. 11. The arrows outgoing from the binary $SiO_2-Al_2O_3$ subsystem mark the compositional lines on which our sample series are located.

Assuming total yttria saturation from the Y-TZP matrix, only the appropriate SiO_2/Al_2O_3 impurity ratio determines the final composition of the intergranular glass phase. The melt composition lowest in Al_2O_3 lies in this ternary system in the sketched part of the phase diagram at about 10 wt. % Al_2O_3 and 50 wt. % SiO_2 (*a* in Fig. 11). This glass composition is in equilibrium with solid SiO_2. For the A series containing SiO_2 additive only, the amount of the ternary glass phase of composition *a* lies at ten times their Al_2O_3 impurity-content in wt. % (10 wt. % Al_2O_3). For the B series, the content of glass of composition designated with *a* corresponds to twice the SiO_2 concentration in wt. % (50 wt. % SiO_2).

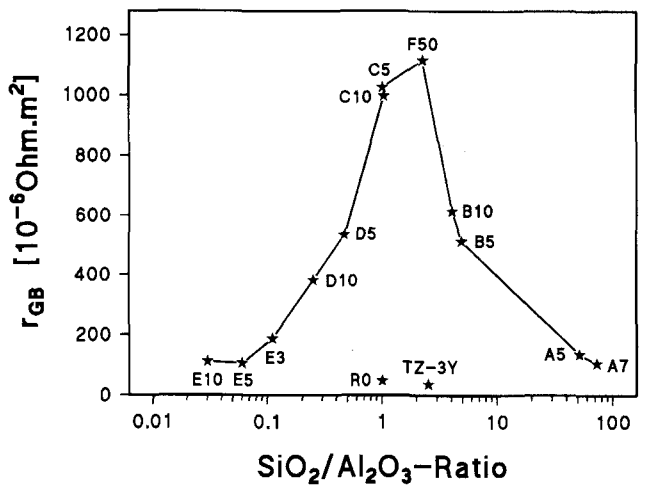

FIG. 10. Normalized grain boundary resistivity at 673 K as a function of the SiO_2/Al_2O_3 ratio.

On the other side of the diagram, the Al_2O_3-rich melt composition which is in equilibria with solid Al_2O_3 is at 35 wt. % Al_2O_3 and 35 wt. % SiO_2 (*b* in Fig. 11). The alumina rich series C, D, and E will form glass of composition *b* in amounts corresponding to about three times their SiO_2 concentration in wt. % (35 wt. % SiO_2). The calculated glass contents of all specimens in wt. % are given in Table IV.

Although the liquidus of the quaternary $SiO_2-Al_2O_3-Y_2O_3-ZrO_2$ system has not yet been elucidated, we can expect an analogous region of glass melts at 1773 K, lying between 10 wt. % Al_2O_3 and 50 wt. % SiO_2 on the SiO_2-rich side and 35 wt. % Al_2O_3 and 35 wt. % SiO_2 on the Al_2O_3-rich side of the quasi-binary edge. This assumption is supported by EDX analysis of glass areas in the triple grain junctions showing systematic variations of the glass phase composition in function of the SiO_2/Al_2O_3 ratio.

From the densities of the bulk 3Y-TZP material and of the $SiO_2-Al_2O_3-Y_2O_3$ glass compositions, we can determine the volume content of the glass phase using the following simplified equation, valid for small concentration of the glass:

$$\text{Vol. \% glass} \cong \text{wt. \% glass} \cdot D_{TZP}/D_{glass},$$

where $D_{TZP} = 6.08$ g/cm^3 is the theoretical density of 3Y-TZP and D_{glass} the density of the glass phase.

The density of the glass phase depends on its composition, and varies especially with the yttria content. For the ternary $SiO_2-Al_2O_3-Y_2O_3$ glass of composition *a* (see Fig. 11) with a content of 10 wt. % alumina, the density is known[54] to be 3.2 g/cm^3; for the alumina rich glass *b* the density[54] is 3.5 g/cm^3. The appropriate volume content of glass can now be calculated for

TABLE IV. Derived specific properties of intergranular glass films at 673 K.

Sample	Glass content		δ_{GB} (eq) (nm)	σ_{GB} (eq) (10^{-6} S/m)	ϵ_{GB} (eq)
	Wt. %	Vol. %			
TZ-3Y	0.015	0.026	0.04	1.11	0.50
R-0	0.09	0.15	0.24	5.00	4.52
A-3	0.10	0.19	0.30	3.13	6.21
A-5	0.10	0.19	0.34	2.52	4.55
A-7	0.10	0.19	0.33	3.14	5.68
B-3	0.46	0.86	1.87	3.41	20.31
B-5	0.78	1.46	2.82	5.50	15.51
B-10	1.52	2.61	5.23	8.52	44.56
C-1	0.18	0.31	0.53	3.25	6.93
C-5	0.75	1.29	2.48	2.41	34.92
C-10	1.41	2.42	4.71	4.72	57.00
D-3	0.27	0.46	0.88	9.67	11.51
D-5	0.45	0.77	1.67	3.29	22.51
D-10	0.57	0.98	1.88	4.93	17.39
E-3	0.09	0.15	0.29	1.55	3.47
E-5	0.09	0.15	0.31	2.95	4.44
E-10	0.09	0.15	0.31	2.79	4.21
F-46	6.30	10.8	18.16	16.27	130.81

each composition from the amount of SiO_2 and Al_2O_3 impurities and is given in Table IV.

Figure 12 shows the normalized grain boundary resistivity at 673 K as a function of the calculated glass content in vol. %. At glass contents of more than 1 vol. %, the intergranular resistivity remains approximately constant (sample series B, C, and D). This indicates that an equilibrium thickness of the intergranular film has already been achieved and the further excess of the glass phase segregated at triple grain junctions and on the surface of the specimens.

From the volume fraction of the glass phase and the average linear grain size l (Table II), the equivalent thickness of the grain boundary layer δ_{GB} (eq) can be calculated. Assuming the total amount of the glass phase is homogeneously distributed between neighboring grains and no segregation in triple points occurs, according to the "brick-layer" model, we obtain that the equivalent thickness of the grain boundary layer, δ_{GB} (eq), is proportional to the ratio of the volume of the glass phase to the volume of the bulk grain material:

$$\delta_{GB}\ (\text{eq}) \cong (a/3) \cdot [\text{vol.\% glass}/(100 - \text{vol.\% glass})] \quad (3)$$

where $a = 1.5l$ is the average cube length and $a/3 = l/2$ is the ratio of the cube volume to the half of the cube surface.[47]

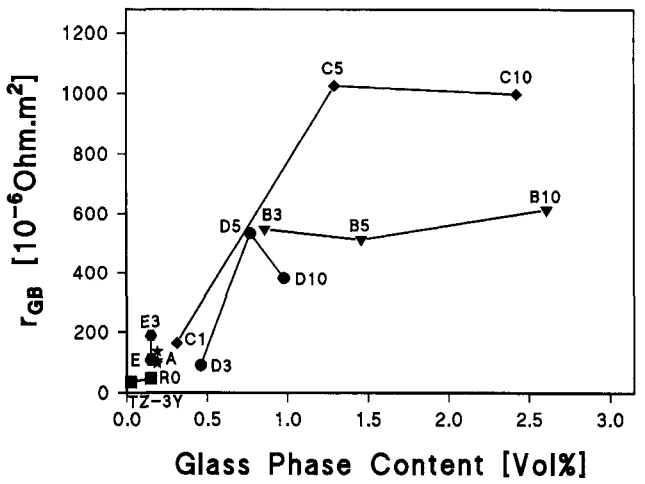

FIG. 12. Normalized grain boundary resistivity at 673 K as a function of the glass content.

The calculated equivalent thickness of intergranular glass films is given in Table IV. Figure 13 shows the dependence of the normalized resistivity at 673 K versus the equivalent film thickness. The threshold for the constant resistivity is found at 1–2 nm. This equilibrium film thickness value corresponds to two to four monolayers of SiO_4-tetrahedra of the dimension of 0.48 nm.

The macroscopic grain boundary resistivities at 673 K as a function of the annealing time at 1773 K are shown in Fig. 14. During the annealing process the macroscopic specific grain boundary resistivities decrease in samples B-10 and C-10, in which the equilibrium thickness of intergranular glass films has already been achieved. On the other hand, in samples having low glass contents (R-0, A-7, C-1, and E-10), the value of the macroscopic grain boundary resistivity remains constant. This behavior can be assigned to the grain coarsening which reduces the number of the grain

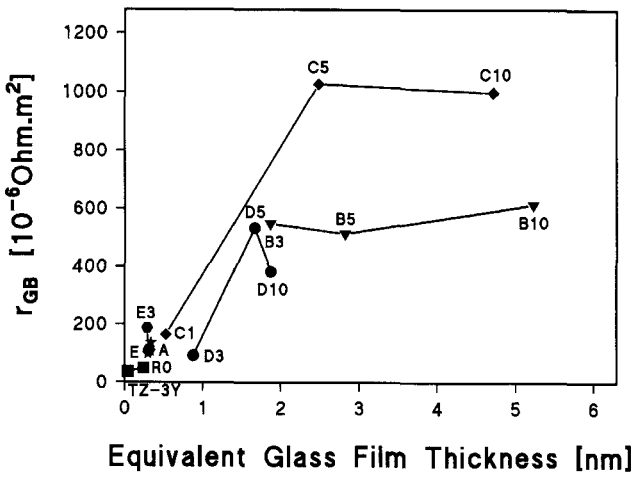

FIG. 13. Normalized grain boundary resistivity at 673 K as a function of the equivalent thickness of the intergranular film.

boundaries perpendicular to the current direction. Only in "saturated" samples the glass phase is squeezed out from the grain boundaries during the grain growth.

D. Specific properties and the equilibrium film thickness

The microscopic specific electrical properties of the intergranular phase, σ_{GB} (eq) and ϵ_{GB} (eq), shown in Table IV, were derived according to Eqs. (1) and (2) from the calculated values of equivalent thickness δ_{GB} (eq) and the experimentally found macroscopic values of ρ'_{GB} and C_{GB} (Table III). The resulting microscopic specific conductivity of the intergranular phase at 673 K varies between 1.1×10^{-6} S/m and 1.6×10^{-5} S/m and the dielectric constant from 0.5 to 130.8 at 693 K. However, at low glass phase contents the estimated equivalent mean thickness is smaller than the expected equilibrium value of 1–2 nm, and a continuous intergranular glass layer cannot be formed. As a result, the current path partially avoids crossing the disjointed glass films and shunt over the "clean" grain boundaries. This parallel current path results in lower values of ρ'_{GB} (Table III) and σ_{GB} (eq), as well as in too low values of ϵ_{GB} (eq) for the samples TZ-3Y, R-0, C-1, and the whole A and E series. On the other hand, for equivalent thicknesses much exceeding the equilibrium width of intergranular films (samples B-10, C-10, and F-46), too high values for σ_{GB} (eq) and ϵ_{GB} (eq) are obtained.

In order to verify these results, we want to compare the specific properties of the glass phase which we found by analyzing the experimental results using the brick layer model with the properties of bulk glass material. Two glasses have been prepared by melting the appropriate amounts of oxides at 1973 K. The first glass with the eutectic composition of the SiO_2–Al_2O_3–Y_2O_3 system (46 wt.% SiO_2, 22 wt.% Al_2O_3, and 32 wt.% Y_2O_3) melts at 1617 K.[44–46] The second glass that was prepared as a bulk sample corresponds to the quaternary composition found in the three grain junctions by EDX analysis (42 wt.% SiO_2, 22 wt.% Al_2O_3, 21 wt.% Y_2O_3, and 15 wt.% ZrO_2).

Figure 15 shows the temperature dependences of the permittivity, ϵ', and Fig. 16 the Arrhenius plots of the conductivities of both glasses. At 693 K the permittivity of the ternary eutectic glass is 7.5 and that of the quaternary glass containing ZrO_2 is 15.7. The corresponding specific conductivities at 693 K are $5.18 \cdot 10^{-7}$ S/m for the ternary glass and $6.34 \cdot 10^{-7}$ for the quaternary one. The activation energies of the electrical conductivities of these glasses are 1.11 ± 0.02 eV and 1.21 ± 0.02 eV, respectively. All these properties are in good agreement with the values of the specific properties of the intergranular glass phase, calculated

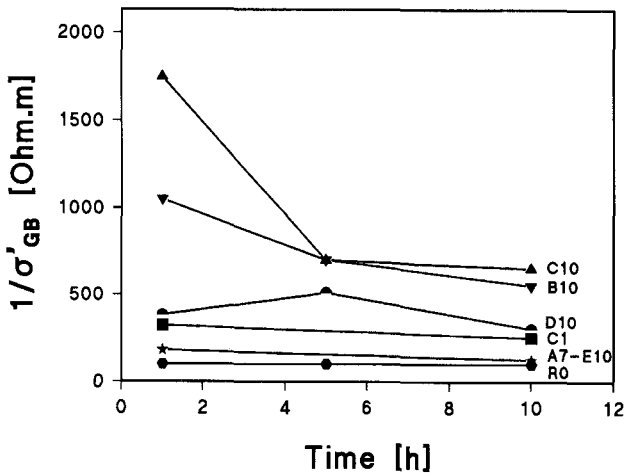

FIG. 14. Macroscopic specific grain boundary resistivity at 673 K as a function of annealing time.

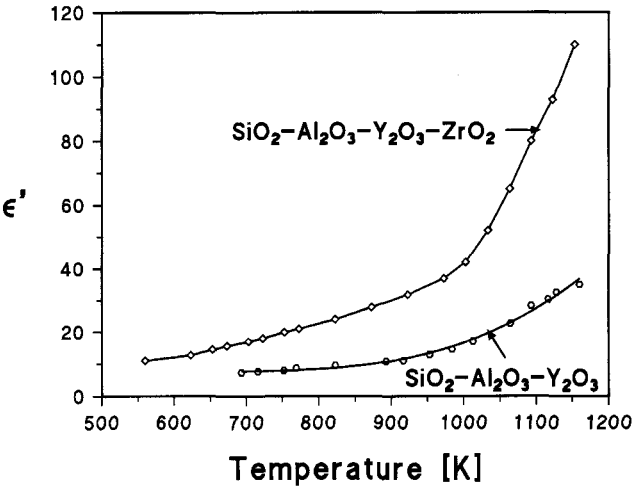

FIG. 15. The temperature dependence of the real part of the complex dielectric permittivity of SiO_2–Al_2O_3–Y_2O_3–(ZrO_2) glasses (for compositions, see text).

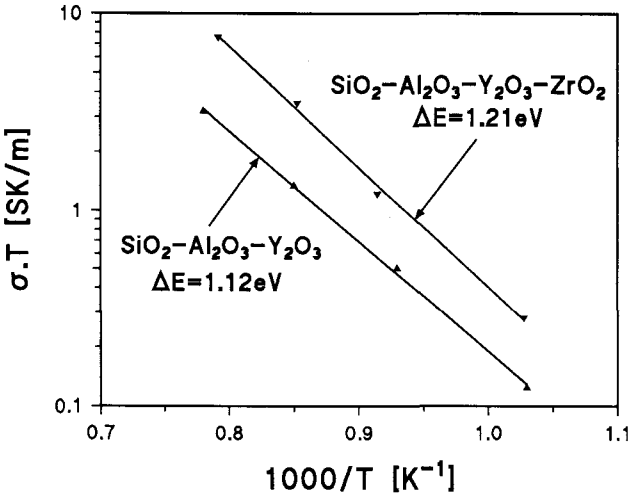

FIG. 16. Arrhenius plots of the electrical conductivities of SiO_2–Al_2O_3–Y_2O_3–(ZrO_2) glasses (for compositions, see text).

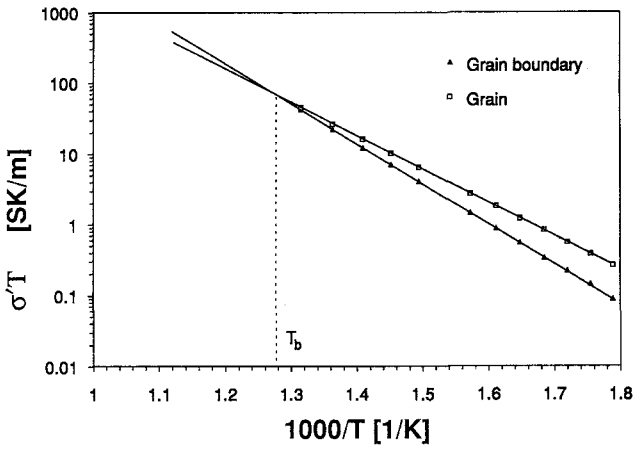

FIG. 17. Arrhenius plots of grain and intergrain conductivities (sample E-1).

from the polycrystalline ceramic samples according to the "brick-layer" model (see Tables IV and V).

E. The characteristic temperature T_b

Typical temperature dependences of both the intragrain and grain boundary conductivity of 3Y-TZP, as determined from ac-impedance spectroscopy for the sample E1, are shown as Arrhenius plots (log $\sigma' T$ against $1/T$) in Fig. 17. The slopes of the Arrhenius plots reveal the corresponding activation energies of σ'. It can be seen that the ionic conductivity of the bulk material (grains), which is almost the same for all samples, has a lower activation energy than the conductivity of the grain boundaries. Consequently, the two Arrhenius lines for the grains and grain boundaries intersect at high temperatures.

TABLE V. Activation energies, the characteristic temperature T_b, and the equilibrium thickness of intergranular glass films.

Sample	ΔE_G (eV)	ΔE_{GB} (eV)	T_b (K)	δ_{GB} (nm)
TZ-3Y	0.94	1.18	615	1.26
R-0	0.93	1.12	650	0.84
A-3	0.93	1.13	1030	0.75
A-5	0.93	1.10	1130	1.17
A-7	0.91	1.12	920	0.92
B-3	0.94	1.14	1360	1.44
B-5	0.92	1.10	3760	1.11
B-10	0.93	1.13	2040	1.24
C-1	0.93	1.15	890	1.19
C-5	0.92	1.12	3520	1.11
C-10	0.92	1.12	3350	1.30
D-3	0.93	1.11	770	1.19
D-5	0.90	1.15	1760	1.17
D-10	0.92	1.10	1430	1.65
E-3	0.93	1.12	1060	1.32
E-5	0.93	1.12	780	1.09
E-10	0.92	1.12	810	1.15
F-46	0.93	1.15	2800	1.95

The temperature at the point of intersection, T_b, which increases with increasing grain boundary film thickness, is the characteristic temperature of the intergranular conductivity blocking, which is caused by the intergranular glass phase films. At temperatures lower than T_b, the macroscopic specific grain boundary resistivity, ρ'_{GB}, exceeds the specific resistivity of the grains, ρ'_G. The total (dc) specific resistivity, ρ'_T, is then determined by the predominating resistivity of grain boundaries ($\rho'_T \cong \rho'_{GB}$). At temperatures higher than T_b, the macroscopic grain boundary resistivity, ρ'_{GB}, becomes negligibly small in comparison to the resistivity of grains, and the total specific resistivity, ρ'_T, reveals the properties of the bulk material ($\rho'_T \cong \rho'_G$).

A change in the slope of Arrhenius plots of total conductivity is observed at the characteristic blocking temperature T_b, at which the low-temperature grain boundary controlled conduction turns into a high-temperature region of lattice-diffusion determined charge transport. At this temperature the macroscopic resistivity of grain boundaries is equal to the macroscopic resistivity of grains, both of which are exactly one-half of the total sample resistivity ($\rho'_{GB} = \rho'_G = 1/2\rho'_T$). This behavior is schematically shown in Fig. 18.

The characteristic temperatures, T_b, of the 3Y-TZP samples (Table V) were determined as the intercept points of the Arrhenius lines of the grain boundary and grain conductivities and are plotted in Fig. 19 versus the equivalent thickness of the glass phase δ_{GB} (eq). A constant saturation value is found if the calculated equivalent thickness of the intergranular film exceeds about 1–2 nm, similar to the results shown in Fig. 13.

The characteristic temperatures, T_b, and the activation energies of the conductivity both within the

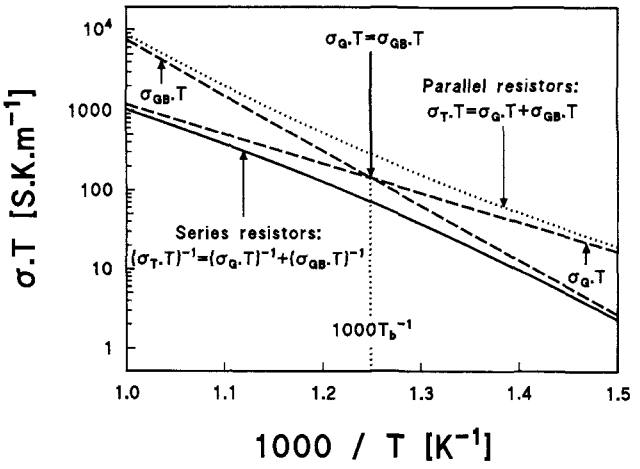

FIG. 18. The transition from the grain boundary to the grain conductivity controlled region (schematically).

grains and in the grain boundaries are given in Table V, together with the equilibrium thickness of intergranular films, δ_{GB}, calculated according to Eq. (2) from the macroscopic grain boundary capacitance C_{GB} (Table III), using the known permittivity of the glass phase of 15.7 at 693 K (see Fig. 15). It can be seen that even the TZ-3Y sample with the least amount of glass shows a T_b of 615 K. The activation energy of the conductivity of the bulk grain material, ΔE_G, is 0.92–0.93 ± 0.02 eV for all samples. The activation energy of the conductivity of grain boundaries, ΔE_{GB}, was found to vary from 1.10 ± 0.02 to 1.18 ± 0.02 eV.

IV. CONCLUSIONS

A change in the slope of the Arrhenius plots of total conductivity toward lower activation energy occurring in 3Y-TZP at a characteristic temperature T_b is caused by an additional resistance of intergranular glass films in series with the bulk material. The thickness of these glass films is limited by a maximum equilibrium value of 1–2 nm. Our results show that the "brick-layer" concept allows one to evaluate the equivalent thickness of intergranular films and even the specific properties of the glass phase.

In order to describe the complex total conductivity behavior of solid ceramic electrolytes, the combined influence of the lattice and microstructural defects, such as dopant atoms, dislocations, grain boundaries, phase segregations, pores and microcracks, which may be present both in series and parallel connections, should be taken into account. The behavior between the stage II and stage III can be modeled by an equivalent *electrical circuit* of two resistors in series: $\rho_T = \rho'_G + \rho'_{GB}$. At low temperatures the macroscopic resistivity of grain boundaries is higher than that of the bulk material, and the charge transport in 3Y-TZP ceramics is suppressed. Due to the higher activation energy, the macroscopic specific resistivity of the grain boundaries decreases with increasing temperature faster than that of the bulk. At the characteristic temperature T_b, the resistivity values of grains and grain boundaries become equal. Above this temperature the resistivity of grain boundaries is negligible and the resistivity of grains determines the total resistivity of the ceramics. On the other hand, if the *parallel electrical circuit* of two resistors would be used, for which the total conductivity is the sum of both conductivity values, the bend in Arrhenius plot would have to occur from the lower to the higher activation energy with increasing temperature. Such behavior is known to exist between the intrinsic stage I and the extrinsic stage II: $\sigma_T = \sigma'_I + \sigma'_E$. However, this high-temperature bend of Arrhenius plots has not yet been observed in doped zirconias, since an appreciable concentration of intrinsic defects is formed only above 2000 K.[55]

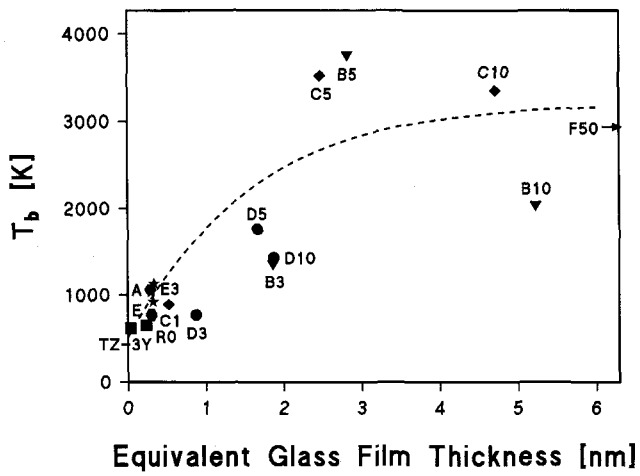

FIG. 19. The dependence of the characteristic grain boundary blocking temperature T_b on the calculated equivalent thickness of intergranular films.

ACKNOWLEDGMENTS

This work was financially supported by the Alusuisse-Lonza Corporation and the Swiss Federal Office of Energy (OFEN). The authors express their gratitude to Dr. L. Dubal from OFEN for his support and continuous interest and Professor P.D. Ownby for helpful discussions and reviewing the manuscript.

REFERENCES

1. A.J.A. Winnubst, P.J.M. Kroot, and A.J. Burggraaf, J. Phys. Chem. Solids **44**, 955 (1983).
2. A.J.A. Winnubst, M.J. Verkerk, and A.J. Burggraaf, in *Advances in Ceramics: Vol. 7*, edited by M.F. Yan and A.H. Heuer (American Ceramic Society, Inc., Westerville, OH, 1983), p. 177.
3. H. Schubert, N. Clausen, and M. Rühle, in *Advances in Ceramics: Vol. 12*, edited by N. Clausen, M. Rühle, and A.H. Heuer (American Ceramics Society, Inc., Westerville, OH, 1984), p. 766.

4. A. J. Burggraaf, M. Van Hemert, D. Scholten, and A. J. A. Winnubst, Mater. Sci. Monogr. **28B**, 797 (1985).
5. R. Chaim, D. G. Brandon, and A. H. Heuer, Acta Metall. **34**, 1933 (1986).
6. R. K. Slotwinski, N. Bonanos, and E. P. Butler, J. Mater. Sci. Lett. **4**, 641 (1985).
7. M. L. Mecartney, J. Am. Ceram. Soc. **70**, 54 (1987).
8. M. J. Verkerk, A. J. A. Winnubst, and A. J. Burggraaf, J. Mater. Sci. **17**, 3113 (1982).
9. M. J. Verkerk, B. J. Middelhuis, and A. J. Burggraaf, Solid State Ionics **6**, 159 (1982).
10. M. Miyayama, H. Yanagida, and A. Asada, Am. Ceram. Soc. Bull. **64**, 660 (1985).
11. S. P. S. Badwal and A. E. Hughes, in *Proc. 2nd Int. Symp. Solid Oxide Fuel Cells*, edited by F. Grosz, P. Zegers, S. C. Singhal, and O. Yamamoto (Commission of European Communities Rep. EUR 13546 EN, Luxembourg, Belgium, 1991), p. 445.
12. D. R. Clarke, in *Mat. Sci. Res. Vol. 21*, edited by J. A. Pask and A. G. Evans (Plenum Press, New York and London, 1987), p. 569.
13. D. R. Clarke, J. Am. Ceram. Soc. **70**, 15 (1987).
14. S. P. S. Badwal and J. Drennan, J. Mater. Sci. **22**, 3231 (1987).
15. R. Raj, J. Am. Ceram. Soc. **64**, 245 (1981).
16. T. Stato, M. Nauer, and C. Carry, J. Am. Ceram. Soc. **74**, 2615 (1991).
17. E. P. Butler and J. Drennan, J. Am. Ceram. Soc. **65**, 474 (1982).
18. J. Drennan, M. V. Swain, and S. P. S. Badwal, J. Am. Ceram. Soc. **72**, 1279 (1989).
19. S. P. S. Badwal, F. T. Ciacchi, M. V. Swain, and V. Zelizko, J. Am. Ceram. Soc. **73**, 2505 (1990).
20. M. J. Verkerk (Ph.D. Thesis, University of Twente, The Netherlands (1982).
21. S. P. S. Badwal, J. Mater. Sci. **19**, 1767 (1984).
22. S. P. S. Badwal, J. Am. Ceram. Soc. **73**, 3718 (1990).
23. D. K. Hohnke, in *Fast Ion Transport in Solids*, edited by P. Vaskista, J. N. Mundy, and G. K. Shenoy (Elsevier North-Holland, Inc., New York, 1979), p. 669.
24. A. Nakamura and J. B. Wagner, J. Electrochem. Soc. **133**, 1542 (1986).
25. M. Weller and H. Schubert, J. Am. Ceram. Soc. **69**, 573 (1986).
26. M. Weller and H. Schubert, in *Solid State Ionics*, edited by M. Balkanski, T. Takahaski, and H. L. Tuller (Elsevier Science Publishers B. V., Amsterdam, The Netherlands, 1992), p. 569.
27. A. S. Nowick and D. S. Park, in *Superionic Conductors*, edited by G. Mahan and W. Roth (Plenum Press, New York, 1976), p. 395.
28. S. P. S. Badwal, J. Mater. Sci. **18**, 3117 (1983).
29. A. Orliukas, B. Heeb, B. Michel, K. Sasaki, P. Bohac, and L. Gauckler, in Proceedings Europ. Ceram. Soc. 2nd Conference, Augsburg, Germany, Sept. 11–14, 1991 (to be published).
30. H. Ohno, T. Nagasaki, T. Ishiyama, Y. Katano, and H. Katsuta, J. Nucl. Mater. **141–143**, 392 (1986).
31. A. S. Nowick, D. Y. Wang, D. S. Park, and J. Griffith, in *Fast Ion Transport in Solids*, edited by P. Vashista, J. N. Mundy, and G. K. Shenoy (Elsevier North-Holland, Inc., New York, 1979), p. 673.
32. F. K. Moghadam, T. Yamashita, and D. A. Stevenson, in *Advances in Ceramics: Vol. 3*, edited by A. H. Heuer and L. W. Hobbs (American Ceramics Society, Inc., Westerville, OH, 1981), p. 364.
33. C. Pascual, J. R. Jurado, and P. Duran, J. Mater. Sci. **18**, 1315 (1983).
34. F. Moztarzadah, Ceram. Int. **14**, 27 (1988).
35. E. C. Subbarao and T. V. Ramakrisnan, in *Fast Ion Transport in Solids*, edited by P. Vashista, J. N. Mundy, and G. K. Shenoy (Elsevier North-Holland, Inc., New York, 1979), p. 653.
36. N. Bonanos, R. K. Slotwinski, B. H. Steele, and E. P. Butler, J. Mater. Sci. Lett. **3**, 245 (1984).
37. M. Kleitz, H. Bernard, E. Fernandez, and E. Schouler, in *Advances in Ceramics: Vol. 3*, edited by A. H. Heuer and L. W. Hobbs (American Ceramics Society, Inc., Westerville, OH, 1981), p. 310.
38. C. G. Koops, Phys. Rev. **83**, 121 (1951).
39. J. E. Bauerle, J. Phys. Chem. Solids **30**, 2657 (1969).
40. A. Orliukas, K. Sasaki, P. Bohac, and L. Gauckler, in *Proc. 2nd Int. Symp. Solid Oxide Fuel Cells*, edited by F. Grosz, P. Zegers, S. C. Singhal, and O. Yamamoto (Commission of European Communities Rep. EUR 13546 EN, Luxembourg, Belgium, 1991), p. 377.
41. R. E. W. Casselton, Phys. Status Solidi A **2**, 571 (1970).
42. P. V. Ananthapadmanabhan, N. Venkatramani, V. K. Rohagi, A. C. Momin, and K. S. Venkateswarlu, J. European Ceram. Soc. **6**, 111 (1990).
43. J. F. Baumard, P. Papet, and P. Abelard, in *Advances in Ceramics: Vol. 24*, edited by S. Sōmiya, N. Yamamoto, and H. Yanagida (American Ceramics Society, Inc., Westerville, OH, 1988), p. 779.
44. S. P. S. Badwal and A. E. Hughes, J. European Ceram. Soc. **10**, 115 (1992).
45. M. Kleitz and J. H. Kennedy, in *Fast Ion Transport in Solids*, edited by P. Vashista, J. N. Mundy, and G. K. Shenoy (Elsevier North-Holland, Inc., New York, 1979), p. 185.
46. L. Dessemond, J. Guindet, A. Hammou, and M. Kleitz, in *Proc. 2nd Int. Symp. Solid Oxide Fuel Cells*, edited by F. Grosz, P. Zegers, S. C. Singhal, and O. Yamamoto (Commission of European Communities Rep. EUR 13546 EN, Luxembourg, Belgium, 1991), p. 409.
47. H. E. Exner and H. P. Hougardy, *Einführung in die Quantitative Gefügeanalyse* (DGM Informationsgesellschaft Verlag, 1986), p. 30.
48. E. E. Underwood, A. R. Colcord, and R. C. Waugh, in *Proc. 3rd Int. Mater. Symposium*, edited by R. M. Fulrath and J. A. Pask (John Wiley and Sons, Inc., New York, 1968), p. 25.
49. T. van Dijk and A. J. Burggraaf, Phys. Status Solidi A **63**, 229 (1981).
50. B. C. H. Steele, J. Drennan, R. K. Slotwinski, N. Bonanos, and E. P. Butler, in *Advances in Ceramics: Vol. 3*, edited by A. H. Heuer and L. W. Hobbs (American Ceramics Society, Inc., Westerville, OH, 1981), p. 286.
51. S. Rajendran, J. Drennan, and S. P. S. Badwal, J. Mater. Sci. Lett. **6**, 1431 (1987).
52. I. A. Bondar and F. Y. Galakhov, Izv. Akad. Nauk. SSSR, Ser. Khim, **7**, 1231 (1964).
53. E. M. Levin, C. R. Robbins, and H. F. McMurdie, *Phase Diagrams for Ceramists* (Supplement, Am. Ceram. Soc., Inc., Westerville, OH, 1969), Fig. 2586.
54. M. J. Hyatt and D. E. Day, J. Am. Ceram. Soc. **70**, C283 (1987).
55. P. Aldebert and J. P. Traverse, J. Am. Ceram. Soc. **68**, 34 (1985).